Development and test of a 500-kV compact Marx generator operating at 100-Hz PRF

Development and Test of a 500-kV Compact Marx Generator Operating at 100-Hz PRF

Laurent Ariztia, Alexey Zhabin, Ivan Lavrinovich, *Member, IEEE*, Antoine Silvestre de Ferron, Marc Rivaletto, Bucur M. Novac, *Senior Member, IEEE*, and Laurent Pecastaing, *Senior Member, IEEE*

***Abstract*— This article presents the electrical and mechanical design of a compact 13-stage 0.5-MV Marx generator operating at a pulse repetition frequency (PRF) of 100 Hz. The fast-switching process of the generator is based on spark gaps, operated under pressurized air and leading to the generation of an output pulsed voltage with a peak of 0.5 MV and a rise time of 15 ns when operated on a 300-Ω load. Corona-stabilized electrodes are installed near the main gap of the switches to improve their operational stability and increase the PRF. To ensure compactness, the Marx generator is housed in a cylindrical metal vessel with a height of 92 cm and an outer diameter of 34 cm, having a total volume of 74 L. A highly accurate simulation using both PSpice and CST software packages was used to predict the impulse waveform at the output of the generator and to help in optimizing the generator design. The tests show a good agreement between the experimental data and the theoretical predictions.**

***Index Terms*— Corona-stabilized switches, Marx generator, pulsed power systems, spark gap switch (SGS).**

I. Introduction

THE conventional Marx generator is recognized as a reliable high-voltage (HV) pulsed power generator, used as a workhorse for many applications over the last decades. However, the significant weight and volume of this type of pulsed HV source limit its application in numerous fields, such as pollution control [1], medical applications [2], or food processing [3]. Usually, such units are too heavy and bulky to be used as a portable pulsed power source [4]. Therefore, the existing interest in low-size generators has attracted more and more attention to the issue of the compact Marx generator design [5]–[17]. Moreover, due to the nature of the abovementioned applications, the generator must have a high pulse repetition frequency (PRF) of at least several tens of hertz to perform an efficient operation. Therefore, the design of modern Marx generators tries downsizing the volume and increasing its PRF, along with facilitating an easy field operation and maintenance. However, fulfillment of all these requirements within one design is not a trivial task, and it requires the application of special mechanical and electrical design considerations.

This article describes the design of a modern, compact, and high PRF 0.5-MV pulsed power Marx generator. Design features are presented in Section II that allow to minimize the volume of the Marx generator and to ensure its stable operation while maintaining its compactness. Section III introduces the details of the highly accurate numerical simulation to predict the performance of the generator, as well as the experimental arrangement, results obtained from the tests, and their comparison with the theoretical predictions. A comparative analysis of the present generator with similar units presented in the literature is presented in Section IV. Finally, a brief section is dedicated to the main conclusions.

II. Marx Design

The Marx generator is one of the basic circuits used for the generation of fast HV impulses. Using the same principle of operation (i.e., parallel charging of capacitors, followed by series discharge), this type of generator can be implemented in various ways: externally triggered or self-triggered, based on very different types of switches [semiconductor or spark gap switches (SGSs)], and finally without housing or with housing filled with dielectric materials, such as oil and/or gas under high pressure.

The mechanical design of the present Marx generator is shown in Fig. 1 and, to avoid an electric field enhancement near sharp edges of the conductive parts, is based on a straight coaxial topology that, for reasons discussed below, and also limits the overall size of the generator. More importantly, during the Marx generator discharge phase, this simpler arrangement makes it easier for the charge to transit between stages, from one block of capacitors to another. Electrostatic simulations were carried out using CST Studio Suite software [18] to calculate the electric field between the

Manuscript received 18 April 2022; revised 11 June 2022; accepted 13 July 2022. This work was supported by the "Investissements d'Avenir," a French program managed by ANR under Grant ANR-16-IDEX-0002, framework of E2S UPPA (PULPA chair). The review of this article was arranged by Senior Editor R. P. Joshi. *(Corresponding author: Alexey Zhabin.)*

Laurent Ariztia, Alexey Zhabin, Ivan Lavrinovich, Antoine Silvestre de Ferron, Marc Rivaletto, and Laurent Pecastaing are with the Laboratoire des Sciences de l'Ingénieur Appliquées à la Mécanique et au génie Electrique–Fédération IPRA, Université de Pau et des Pays de l'Adour/E2S UPPA, 64000 Pau, France (e-mail: laurent.pecastaing@univ-pau.fr; alexey.zhabin@univ-pau.fr).

Bucur M. Novac is with the Laboratoire des Sciences de l'Ingénieur Appliquées à la Mécanique et au génie Electrique–Fédération IPRA, Université de Pau et des Pays de l'Adour/E2S UPPA, 64000 Pau, France, and also with the Wolfson School of Mechanical, Electrical and Manufacturing Engineering, Loughborough University, Loughborough LE11 3TU, U.K.

Color versions of one or more figures in this article are available at https://doi.org/10.1109/TPS.2022.3192286.

Digital Object Identifier 10.1109/TPS.2022.3192286

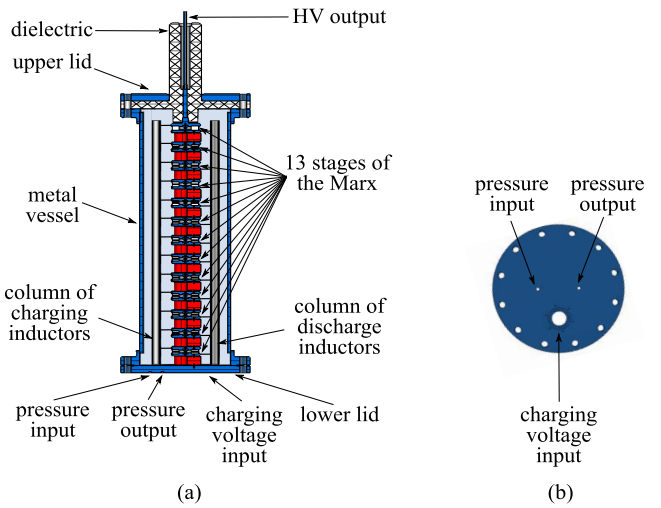

Fig. 1. Mechanical design of the Marx generator. (a) Cross section. (b) View from below.

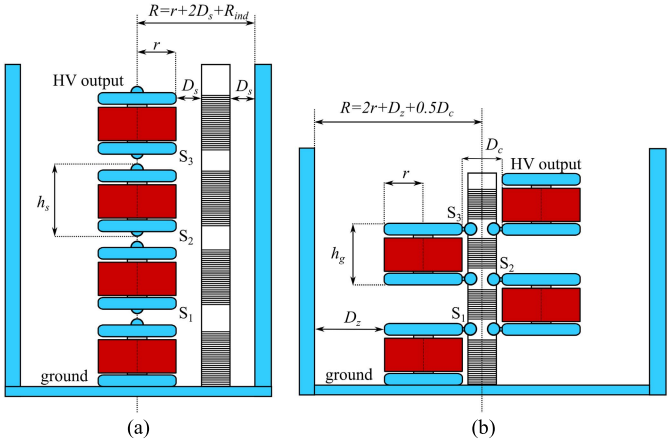

Fig. 2. Possible topologies for mounting the Marx generator's stages. (a) Forming a straight coaxial with the outer housing. (b) Zigzag mounted inside a cylindrical housing. For simplicity, only the discharge column of inductors is shown.

various parts raised to HV and the grounded metallic housing. The geometrical dimensions of these elements have been chosen to ensure that the electric field is below the breakdown value of the air. This value is calculated by the formula [19]: $E_{\text{br}} = 24.5\ p + 6.7(p/R_{\text{eff}})^{0.5}$, where p is a pressure in bars and R_{eff} is a coefficient taking the value 0.23 for the cylindrical shape electrodes. E_{br} equals 195 kV/cm for the pressure of 6.5 bars required to generate a 500-kV impulse.

The cylindrical housing of the Marx generator is represented by a thick stainless-steel cylinder, with an external and internal diameters of 340 and 317 mm, respectively, and a height of 920 mm corresponding to a volume of 74 L. Two heavy lids, also made of stainless steel, are installed at the two ends to allow pressurizing the volume up to seven bars. The bottom lid has service access ports for a pneumatic input and output to control the pressure and for an HV charging cable that uses an Essex bespoke HV connector. The Marx is charged with a positive polarity voltage. A cylindrical dielectric piece of polyethylene is installed in a socket of the upper lid to avoid a breakdown between the HV output and the grounded metallic housing. Its dimensions were very carefully determined for avoiding surface flashover, with a dedicated study being presented elsewhere [20].

As can be seen from Fig. 1, no additional insulating support is used in the mechanical assembly of the Marx generator. The self-supporting structure of the generator has a significant advantage in terms of reliability, as it not only minimizes the risks of losses due to surface electric flashover but also simplifies servicing and reduces the overall weight.

A. Discussion on Straight Coaxial and Zigzag Topologies

The two most common topologies for the stage arrangement of a Marx generator, straight and zigzag [5], are illustrated in Fig. 2, with both topologies having cylindrical geometry. As can be seen from the figure, the generator with the straight coaxial topology is slightly longer, due to the way the electrodes of the SGSs are mounted. However, since two columns of stages need to be installed within the zigzag topology, the radius of the cylindrical housing increases significantly in comparison with the straight coaxial topology. Related to Fig. 2(a), for the straight topology, the radius of the housing R is the sum of the radius of the stage r and the diameter of the inductor $2R_{\text{ind}}$ and two times D_s, where D_s is the distance between the inductor column and both the stage body and housing. Related to Fig. 2(b), for the zigzag topology, the radius of the housing R is the sum of $2r$, the distance between a stage and the housing D_z and a half of the intercolumn distance dc. To reduce the size of the generator, the charging and discharging columns of inductors can be isolated with a dielectric coating, covered with a silicon compound or casted into epoxy resin. In this way, the distance D_s between the columns and the housing can be taken much shorter than the distance D_z between a stage and the housing (see Fig. 2).

When mounted in straight coaxial topology, the SGSs have less parasitic inductance than when mounted in zigzag topology. This both reduces the switching time and the rise time of the generated voltage impulse.

The important advantage of the zigzag topology is that the ultraviolet light generated by the first stage SGSs facilitates the switching of the later ones, i.e., the SGSs "see" each other. In the design of the present compact Marx generator, this feature has been sacrificed to maintain a small volume. Therefore, for the stable operation of the generator, it was necessary to implement in the SGSs a supplementary technique: a corona-stabilized electrode.

B. Single-Stage Design

The efficient operation of a Marx generator is dependent on the proper closing of all SGSs. In the present design, SGSs use pressurized air, with the electrodes made of stainless steel with their hemispherical geometry having a diameter of 22 mm. The interelectrode gap distance for the first SGS is only $d_1 = 2$ mm, the short gap allowing the generation of a quasi-uniform electric field between the electrodes. A single-stage design, showing the distribution of the interelectrode

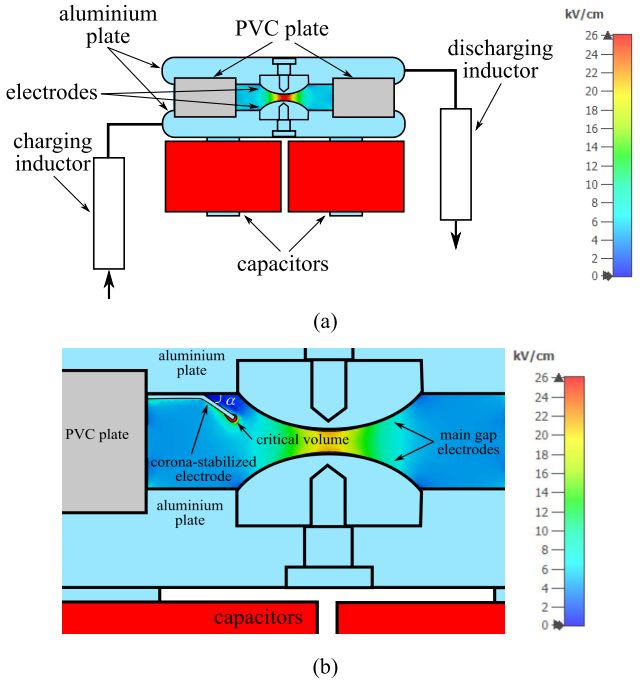

Fig. 3. Cross section of a single-stage. (a) Overall view showing the interelectrode electric field distribution. (b) Details of the corona-stabilized electrode design.

field, is presented in Fig. 3(a). The electrostatic simulation is obtained using the CST software [18]. The difference in potential between the electrodes considered in the numerical simulation is equal to the self-breakdown voltage (i.e., 7.6 kV) of the main interelectrode gap at a pressure of 1 bar. The quasi-uniform electric field allows the SGS to operate at a high breakdown voltage and to better distribute the erosion across the surface of its electrodes. The short gap also reduces the characteristic resistance and inductance during operation and improves the closing time.

The SGS interelectrode gap distance of all the other stages is larger to ensure their sequential switching. When mounted, the interelectrode SGS gaps d_i increase according to $d_i = d_1 + \delta + \gamma \cdot (i - 1)$, where $\delta = 0.7$ mm, $\gamma = 0.1$ mm, and $i = 2, 3, \ldots, 13$. The distance δ was added to make sure that the first SGS closes first.

Each stage consists of three parallel-mounted 1300-pF capacitors, each having a maximum charging voltage of 50 kV. These compact capacitors have low inductance (100 nH) due to their ceramic structure (strontium titanate). When fully erected, the 13-stage Marx generator has a self-inductance of approximately 815 nH and an equivalent capacitance of 300 pF. The precise interelectrode distance is obtained using a polyvinyl chloride (PVC) separation cylinder with a dielectric constant of 2.7 and with holes drilled into it for allowing sufficient flow of air during operation. The plates into which the SGS steel electrodes are mounted are made of aluminum.

C. Corona-Stabilized Electrode Design

As mentioned above, the main disadvantage of the straight coaxial topology is that SGSs cannot "see" each other and ultraviolet light generated by the first few stages cannot facilitate the switching of the later ones. To overcome this disadvantage, corona-stabilized electrodes were installed in the SGSs in stages from 2 to 10. The application of this technique allows to improve the stability of the SGS operation and increases the PRF of the generator [21].

Referring to Fig. 3(b), one side of the corona-stabilized electrode is fixed onto the upper electrode, dc grounded through the discharging inductor column. As shown in Fig. 3(b), the other end of the electrode is mounted toward the HV electrode, making an angle α with the plane of the grounded electrode. The electric field distribution near the corona-stabilized electrode is also presented in Fig. 3(b). The applied voltage (5.8 kV) is lower than the self-breakdown voltage of the gap in atmospheric air to see the field before the breakdown. The difference in potential applied between the sharp edge of the corona-stabilized electrode and the HV electrode produces a highly nonuniform electric field that establishes a corona discharge, creating a region of ionization. This initial cloud of electrons greatly increases the probability of subsequent discharge and minimizes the statistical time lag in the breakdown process [22].

A few electrons can hardly cause an electron avalanche when their position is too far from the corona stabilizing electrode to be accelerated enough to obtain sufficient kinetic energy. A critical volume is defined here as a region close to the highly stressed corona stabilized electrode, where the presence of just a few electrons will lead to an electron avalanche [21]. Ionization in atmospheric air starts when the field strength exceeds 26 kV/cm [23]. Thus, the approximate boundary of the electron cloud lies in red color in Fig. 3(b). The distance between the electron cloud and the HV electrode is 9 mm. The location of the critical ionization volume, the degree of the field enhancement, and its distribution near the sharp end of the corona-stabilized electrode can all be adjusted by changing the angle α and/or the distance between the HV electrode and the critical volume [see Fig. 3(b)]. The electrical field strength in this region should be low enough, such that breakdown will not occur while charging the capacitors but will occur when the voltage impulse from the previous stages will be applied across the interelectrode gap.

Since the corona phenomena occur before the complete breakdown of the gap, the corona stabilization effect will act on any of the subsequent breakdowns during the PRF operation. Therefore, an improvement in the insulation recovery performance of the interelectrode gas and a reduction of the breakdown voltage jitter are both expected, as detailed in [21]. Preliminary testing of the 13-stage Marx generator proved that, after setting the optimum positions for all the corona-stabilized electrodes, it has a very stable operation even in atmospheric air. After this successful preliminary testing, the generator was mounted inside the pressurized metal housing.

As mentioned in [21], the application of the corona stabilized electrode reduces the breakdown delay. It also reduces the jitter of the generator. A supplementary study was conducted to estimate the degree of this improvement for a single SGS in atmospheric air. The gap distance was set to 2 mm and the applied voltage was 7.2 kV. A series of 150 pulses were

applied to the SGS without the corona-stabilized electrode and with it deflected at an angle $\alpha = 30°$ (high field inhomogeneity) and an angle $\alpha = 5°$ (low field inhomogeneity). The value of the standard deviation of the breakdown delay in the SGS without the corona-stabilized electrode is 7.2 μs, while with the needle electrode, it is 1.6 and 0.59 μs for low and high field inhomogeneity, respectively. Thus, it can be concluded that the application of the corona stabilized electrode reduces the delay time of the SGS, and this effect is enhanced with an increase in the degree of field inhomogeneity in the vicinity of its end.

D. Columns of Inductors

The charging and discharging circuits have the same design, which includes two hand-made columns of stacked inductors. The role of the charging column is to reduce the energy losses and to allow the required fast charging of the capacitors to obtain the high PRF required from the generator. Each inductor is designed to have a sufficient number of turns to withstand the electric stress during charging and discharging.

The fall time constant of the voltage impulse must be long enough to guarantee the closing of the switch in the next stage of the generator since it determines the overvoltage time on the gap electrodes. The overvoltage time on SGSs is important for its stable operation due to the statistical and formative delays associated with the gas breakdown process [24]. The fall time constant can be raised by increasing the self-inductance values of the charging and discharging inductors. However, this will lead to a growth in the generator's size. Thus, to find a compromise between compactness and stable operation of the generator, for different stages, the dimensions of inductors are different.

Because the overvoltage on the gap electrodes for the first three stages of the generator is lower than that applied on the other, a higher value of charging and discharging inductors is required. Thus, the self-inductance of the first three stages is $L_i = 145$ μH, for $i = 1, \ldots, 3$, while the rest of the inductors have a self-inductance $L_j = 104$ μH for $j = 4, \ldots, 13$. An assembled column has a diameter of 40 mm, with inductors type L_i measuring 95 mm in height, while the inductors L_j measure 70 mm. Most of the inductors are made using a wire with a thickness of insulation of only 0.2 mm. However, to avoid undesirable breakdown to the housing, the inductors for the last three upper stages of the Marx generator are casted in a silicone compound.

III. Numerical Simulation and Test Results

To perform a high-precision simulation of the Marx generator discharge at a very high time rate-of-change, all the stray elements (i.e., self-inductance and capacitance, as well as mutual inductance and capacitance) present inside the generator need to be taken into account. Unfortunately, CST, one of the best modern commercial electromagnetic simulation programs, does not contain in its material data library the electrophysical properties of all required materials in the gigahertz range. However, it contains a schematic module supporting the SPICE simulation tool, within which the SGS model can be

Fig. 4. SGS circuit.

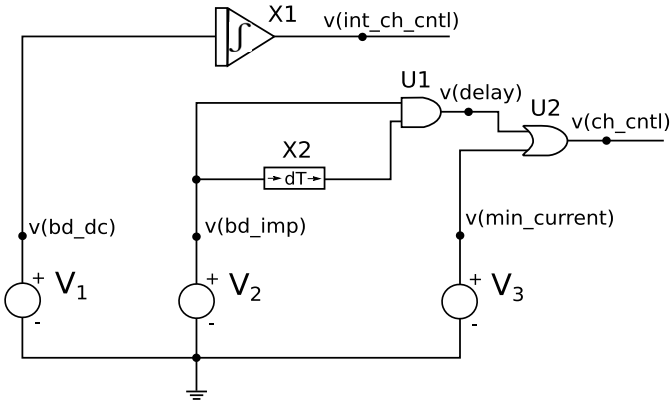

Fig. 5. SGS plasma channel control circuitry.

implemented. The present approach to numerically simulating the generator consists therefore of two parts. The first part estimates the electrophysical properties (i.e., the characteristics of all the stray passive elements) of the geometry under study and represents them as a block of complete S-parameter matrices. The second part allows to conduct circuit transient simulation with an automatically created equivalent circuit of the 3-D electromagnetic (EM) structure and both linear and nonlinear circuit elements of the SGS model.

A. SGS Modeling

The circuit model of the SGS is based on the work reported in [25]. The adopted physical model predicts the behavior of an SGS using the values of the gas pressure and gap length as inputs. The corona stabilized electrode is not explicitly taken into account, but it is implemented using a zero value for both the statistical time lag and for the self-breakdown dispersion. The basic circuit of the SGS, as shown in Fig. 4, consists of two terminals representing the face of each electrode of the gap and two main elements, where R_{arc} is the resistance and L_{arc} is the self-inductance of the plasma channel. All quantities in the expressions below are presented in SI units.

R_{arc} in turn represents a sum of two resistances: R_{id} and R_{br}. R_{id} models the transition that occurs when a channel initially forms across the entire gap with its value is calculated as $R_{\text{id}} = R_{\text{OFF}}(1 - \text{v(ch\_cntl)})$, where R_{OFF} is the resistance in the nonconductive state ($R_{\text{OFF}} = 1$ MΩ) and v(ch_cntl) is the channel control signal described below. R_{br} is the resistance calculated using the following formula: $R_{\text{br}} = d/(\pi \sigma a^2)$ [26], where d is the interelectrode distance and $a(t)$ is the radius of the plasma arc calculated by the Braginskii formula [26].

The self-inductance L_{arc} is calculated as

$$L_{\text{arc}}(t) = 2d(\ln(2d/a(t)) - 0.75)10^{-9}.$$

The schematic of the part of the model to generate a control signal v(ch_cntl) is shown in Fig. 5. The output voltage of the source V_1 generates a true logical signal if the potential

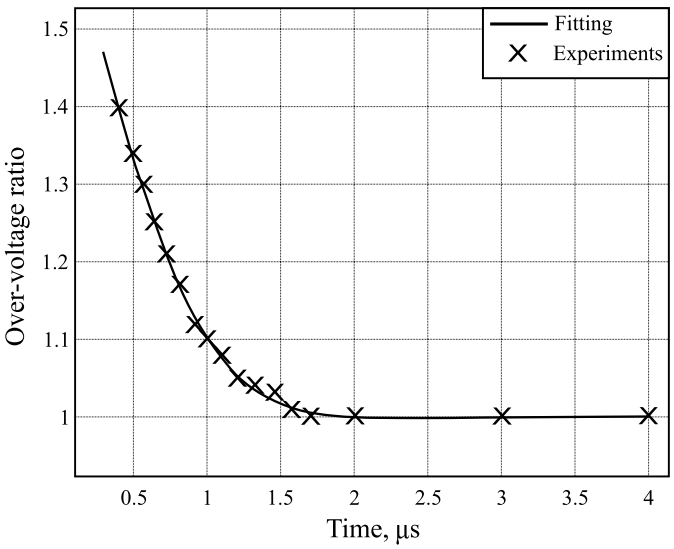

Fig. 6. Relationship between the overvoltage ratio and the prebreakdown delay. The points are representing data from [20], while the line represents a Gaussian fitting curve.

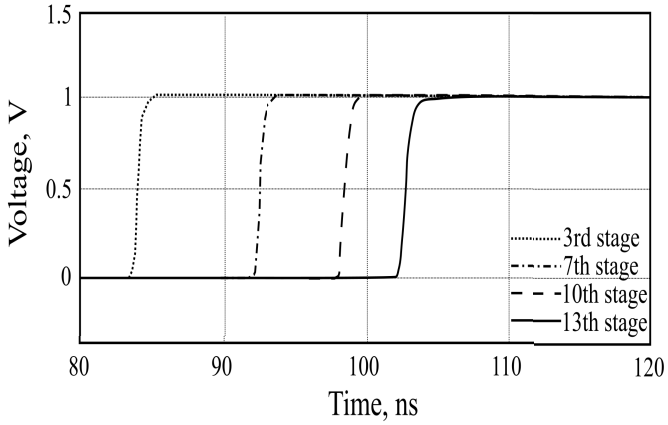

Fig. 7. Waveforms of the channel control signal.

difference between the electrodes exceeds the static breakdown voltage calculated by Paschen's law [25]. In our generator, the closing of an SGS from 2 to 13 occurs when an impulse voltage is applied, for which the breakdown value is higher than the dc value. Thus, the output signal of V_1 is integrated over time to determine the duration of the impulse overvoltage. Experimental data from [27] were used to obtain the relation between the overvoltage ratio and the prebreakdown delay. The data were successfully fit with a Gaussian function (see Fig. 6). The voltage source V_2 generates a true logical signal if the potential difference between the electrodes exceeds the impulse breakdown voltage calculated using the curve from Fig. 6.

The breakdown between the two electrodes occurs after a prebreakdown delay. This time delay is considered to be between the moment at which the gap voltage exceeds the breakdown voltage and the moment at which the channel forms and conduction begins. As can be seen from Fig. 5, the signal v(bd_imp) is multiplied by its delayed version to take into account the prebreakdown delay and to form the signal v(delay). If this signal is true, v(ch_cntl) is also true and an abrupt decrease of R_{arc} takes place, the voltage across the spark gap rapidly collapses, and the current begins to flow. The minimum value of the gap current (I_{min}) that keeps the channel in a conducting state was introduced in the model as a user predefined parameter. The voltage source V_3 generates a true logical signal if the current through the gap exceeds the user's predefined value. Therefore, the logical sum of the v(delay) and v(min_current) signals generates the gap control signal v(ch_cntl).

The waveforms of the channel control signal v(ch_cntl) are presented in Fig. 7. It is easy to note that, due to the channel control circuit, the SGSs do commute sequentially.

B. Numerical Simulation

The schematic of the circuit model of the Marx generator is shown in Fig. 8. The S_j represents the SGS model described above. The index $j = 1, \ldots, 13$ represents the stage number. The block with the complete S-parameter matrices was calculated using the CST 3-D EM solver. It has outputs corresponding to all SGSs electrodes. This block takes into account all stray elements of the geometry under study.

Since the processes of capacitor charging and their discharge through the load (impulse generation) operate in very different time domains (i.e., tens of milliseconds and hundreds of nanoseconds, respectively), two separate schematic simulations were carried out. A simple model of the Marx generator during the charging phase allows us to observe charging time and the nominal voltage at all capacitors. In this model, SGSs are considered as an open circuit.

In the model of SGS operation, the process of charging all capacitances is neglected as it has little effect on the generator's performance. It is simply assumed that at the moment the simulation begins, all stage capacitors C_i are charged to an initial voltage representing 98% of the self-breakdown voltage of the first SGS. At this moment, a trigger voltage pulse is supplied from the impulse voltage source V_{in} through the input separating capacitor C_{in} to charge the capacitor representing the first stage up to the breakdown voltage and thus force the first stage SGS to close.

The generated output voltage impulse applied on the load is compared in Fig. 9 with experimental data. The figure demonstrates a very good agreement between the experimental data and the theoretical predictions. Therefore, the model presented above can be used for the design of highly optimized Marx generators.

C. Test Results

The practical arrangement used in testing the Marx generator is presented in Fig. 10. It consists of four main parts: the trigger generator, the charger, the Marx generator body, and the load. A 50-kV–160-mA Technix charger is used to dc charge the Marx generator. The charger supplies the capacitors with a positive voltage in a trigger mode (inhibit mode) under the control of a trigger pulse generator Keysight 33600A.

Using air pressurized to 6.5 bars and with the charging voltage of the Marx generator set at 39 kV, the generated

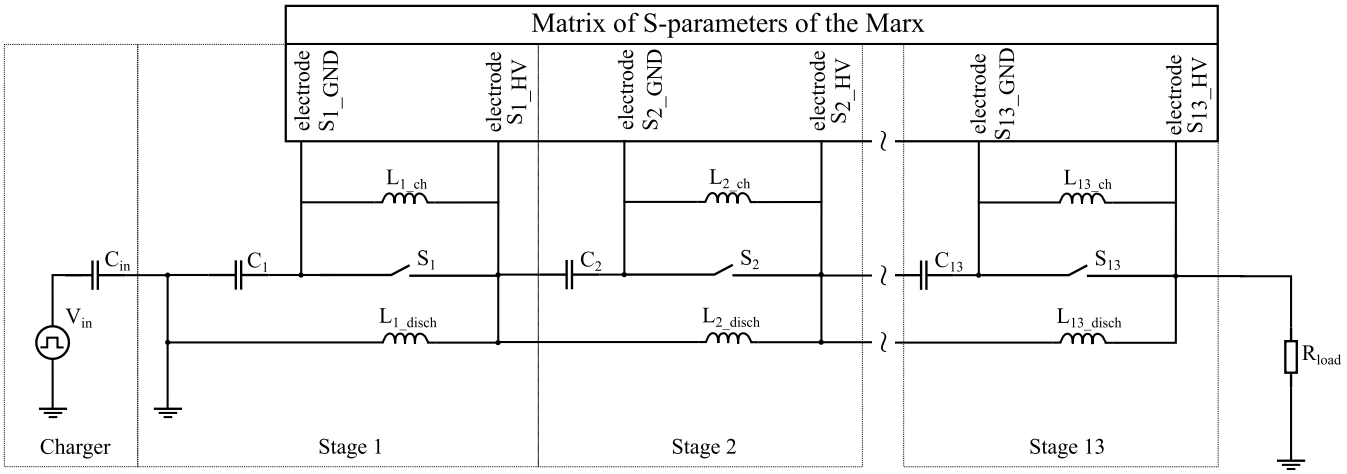

Fig. 8. Circuit model for the Marx generator.

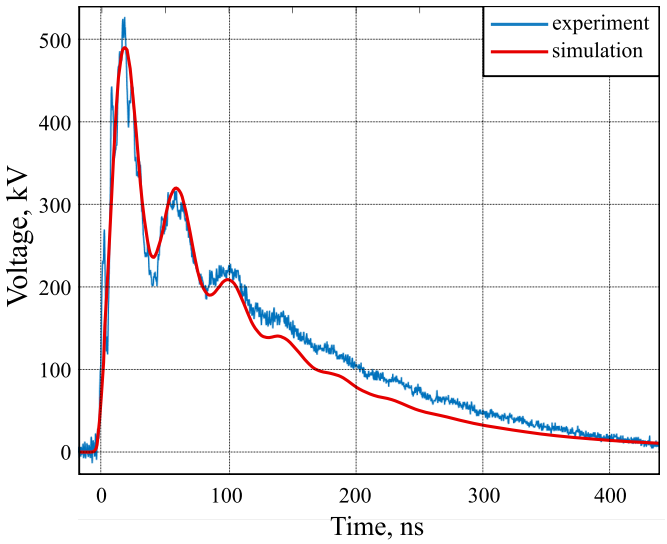

Fig. 9. Impulse waveform on the load for single-mode operation.

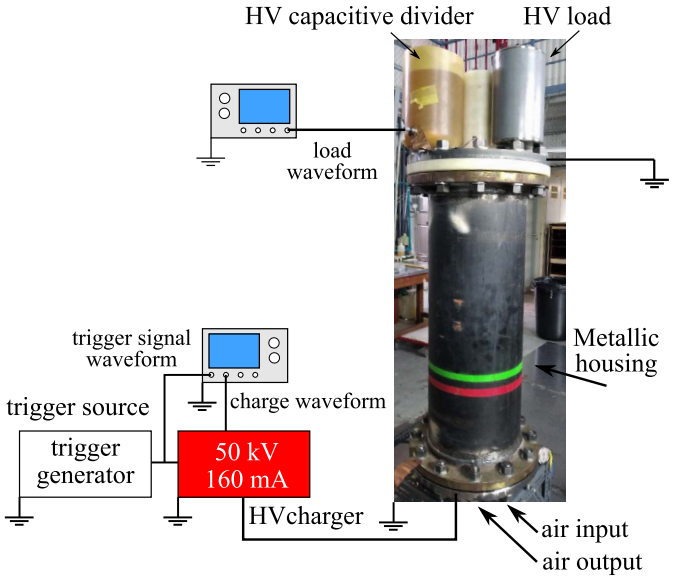

Fig. 10. Block diagram of the practical experimental arrangement for testing the Marx generator.

voltage peak is about 500 kV on a 300-Ω cylindrical water-filled load. The output voltage is measured with a high-quality, ultracompact 0.5-MV capacitive voltage divider [28], having an exceptionally high upper bandwidth limit of 55 MHz for such a unit. The voltage impulses are recorded and analyzed using a Tektronix TDS3052B digital oscilloscope, having a bandwidth of 500 MHz and a sampling frequency of 5 GS/s, placed in a Faraday cage and powered by a UPS.

When tested in the single-shot mode, the Marx generator produced a 500-kV HV impulse delivered to the load with a rise time of 15 ns and a pulsewidth of 70 ns, as shown in Fig. 9. The shot-to-shot variation of the peak voltage and its characteristic rise time is less than ±5% and ±6.3%, respectively.

The generator was also tested in burst mode, with a burst having 100 discharges at a repetition rate of 50, 75, and 100 Hz. The number of impulses is determined by the requirement of our research project (ESCAPADE). The failure rate at a PRF of 50 and 75 Hz does not exceed 5%, while at a PRF of 100 Hz, the rate increases to 15%. However, no irreversible damage was observed and the generator continued to work. Implementation of a system to allow blowing the inner housing air would probably reduce the number of failures at PRF 100 Hz.

Fig. 11(a) and (b) shows the waveforms recorded during a burst of 1 s at a PRF of 100 Hz, with a voltage peak of 450 and 500 kV, respectively. As can be seen from the figure, there is no significant difference between impulses with a peak of 450 kV generated in the burst mode and a corresponding impulse in the single-shot mode. The difference in rise time and amplitude does not exceed the value of the shot-to-shot variation observed in the single-shot mode. However, the variation of the main discharge characteristics is higher when

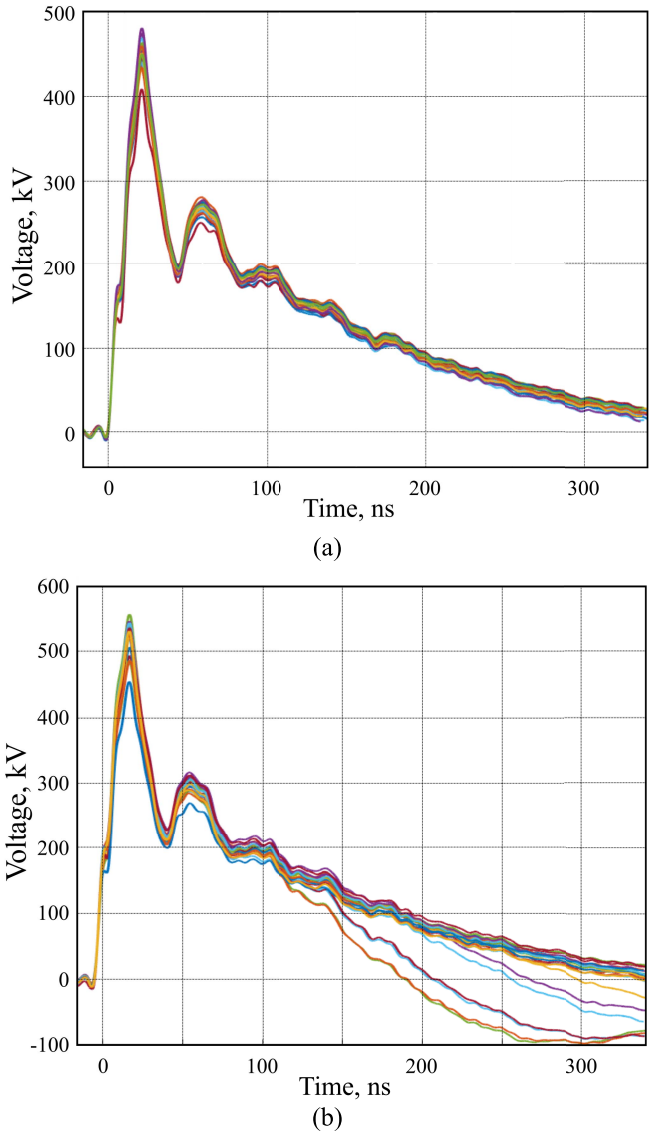

Fig. 11. Impulse waveforms recorded during the burst-mode operation. (a) Overlay of 20 pulses with a peak of 450 kV. (b) Same as (a) but for a peak reaching 500 kV.

the peak reaches 500 kV. Thus, this value of the amplitude is the upper limit for the stable operation of the generator under a PRF of 100 Hz.

The self-breakdown voltage jitter was estimated as a standard deviation of breakdown voltage for a burst of impulses: STD = 28.07 kV. Fig. 12 shows a histogram constructed for a burst of 100 consecutive pulses when the generator is operating at a PRF of 100 Hz. This figure allows to estimate the probability of generating pulses of various peak voltages. As can be seen from the figure, the mean value of the peak voltage is near 520 kV, and the most probable generation of a pulse is in the range of ±45 kV relative to its mean value.

IV. Discussion

The established parameters of the Marx generator are listed in Table I. For comparison, the parameters of other generators of the same class presented in the open literature [7]–[11] are also presented in Table I. It is worth to note that each HV generator has a unique and sometimes bespoke design, and therefore, it is not completely relevant to compare these units.

We note however that the use of SF_6 makes it possible to reduce the size of the generator. However, this gas becomes toxic when used in SGSs and is not allowed by law to be released in the atmosphere, making its use very complicated, with most designers of modern Marx generators trying to avoid using it. We also note that very HV pulsed generators operate at relatively modest repetition rates. As Table I shows, the present generator is one of the most compact among the generators presented, having also the shortest rise time and the highest operational PRF.

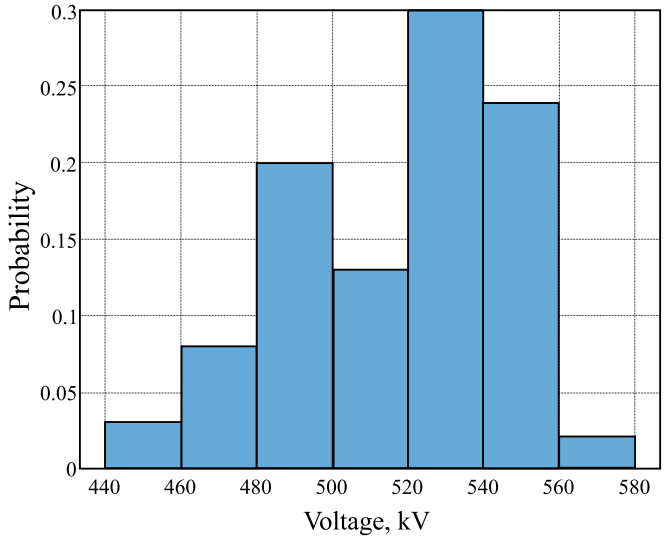

Fig. 12. Histogram of the peak impulse recorded during a burst of 100 shots performed at a PRF of 100 Hz.

TABLE I
Main Characteristics of Marx Generators

	Reference number					
	[7]	[8]	[9]	[10]	[11]	**This paper**
Peak voltage, kV	500	700	700	500	600	**500**
Volume, L	-	300	250	198	199	**74**
Weight, kg	56	-	170	-	170	**226**
Rise-time, ns	20	43	25	50	90	**15**
PRR, Hz	30	5	50	10	-	**100**
FWHM, ns	100	132	200	200	-	**70**
Gas	SF_6/H_2	SF_6	Air	Air	Air	**Air**
Number of stages	22	16	8x20	25	30	**13**
Load, Ohm	59	14	60	18.5	25	**300**

V. Conclusion

This article presents all the details of the design procedure and testing of a compact half-megavolt, high PRF Marx generator. The results of the tests demonstrate that a 13-stage Marx generator, with an output voltage of 500 kV and a stable operation at a PRF of 100 Hz can be accommodated in a

compact volume of only 74 L. The results were achieved using a straight coaxial topology, implementing a corona-stabilized electrode technique and manufacturing charging, and discharging columns from inductors with optimum values. The detailed numerical simulation, using different software packages, accurately determined the optimum parameters of the generator and it also allowed to predict with high accuracy the waveform of the output voltage impulse. The experiments demonstrated that the Marx generator performance is stable both in single-shot mode and in burst mode at a PRF of 100 Hz.

REFERENCES

[1] A. J. M. Pemen, V. R. Chirumamilla, F. J. C. M. Beckers, W. F. L. M. Hoeben, and T. Huiskamp, "An SDBD plasma-catalytic system for on-demand air purification," *IEEE Trans. Plasma Sci.*, vol. 46, no. 12, pp. 4078–4090, Dec. 2018, doi: 10.1109/TPS.2018.2855402.

[2] N. Ibrahimi *et al.*, "A subnanosecond pulsed electric field system for studying cells electropermeabilization," *IEEE Trans. Plasma Sci.*, vol. 48, no. 12, pp. 4242–4249, Dec. 2020, doi: 10.1109/TPS.2020.3034286.

[3] B. M. Novac *et al.*, "Demonstration of a novel pulsed electric field technique generating neither conduction currents nor Joule effects," *IEEE Trans. Plasma Sci.*, vol. 42, no. 1, pp. 216–228, Jan. 2014, doi: 10.1109/TPS.2013.2293915.

[4] A. Rajabi-Nezhad, A. A. Razi-Kazemi, M. Soheyli, and F. Malekipour, "Assessment of different compact Marx generator structures on the voltage profile," *IEEE Trans. Plasma Sci.*, vol. 48, no. 1, pp. 189–195, Jan. 2020, doi: 10.1109/TPS.2019.2955634.

[5] F. Lassalle *et al.*, "Development and test of a 400-kV PFN Marx with compactness and rise time optimization," *IEEE Trans. Plasma Sci.*, vol. 46, no. 10, pp. 3313–3319, Oct. 2018, doi: 10.1109/TPS.2018.2837344.

[6] K. Rainwater, D. Barnett, C. Lynn, J. Dickens, A. Neuber, and J. Mankowski, "A 160 J, 100 Hz rep rate, compact Marx generator for driving and HPM source," in *Proc. IEEE Int. Power Modulator High Voltage Conf. (IPMHVC)*, Jul. 2016, pp. 228–230, doi: 10.1109/IPMHVC.2016.8012819.

[7] H. Zhang, T. Shu, S. Liu, Z. Zhang, L. Song, and H. Zhang, "A compact modular 5 GW pulse PFN-Marx generator for driving HPM source," *Electronics*, vol. 10, no. 5, p. 545, Feb. 2021, doi: 10.3390/ELECTRONICS10050545.

[8] S. Hao, W. Dai, L. Geng, C. Feng, and L. Cao, "Research of compact repetitive pulsed power system based on Marx generator," in *Proc. IEEE 21st Int. Conf. Pulsed Power (PPC)*, Jun. 2017, pp. 1–4, doi: 10.1109/PPC.2017.8291292.

[9] C. Nunnally, M. Lara, J. R. Mayes, W. C. Nunnally, and D. Kohlenberg, "A compact 700-kV erected pulse forming network for HPM applications," in *Proc. IEEE Pulsed Power Conf.*, Jun. 2011, pp. 1372–1376, doi: 10.1109/PPC.2011.6191618.

[10] A. A. Neuber, Y. J. Chen, J. C. Dickens, and M. Kristiansen, "A compact, repetitive, 500 kV, 500 J, Marx generator," in *Proc. IEEE Pulsed Power Conf.*, Jun. 2005, pp. 1203–1206, doi: 10.1109/PPC.2005.300570.

[11] C. Nunnally, J. R. Mayes, C. W. Hatfield, and J. D. Dowden, "Design and performance of an ultra-compact 1.8-kJ, 600-kV pulsed power system," in *Proc. IEEE Pulsed Power Conf.*, Jun. 2009, pp. 930–933, doi: 10.1109/PPC.2009.5386232.

[12] L. Pecastaing *et al.*, "Compact self-loaded Marx generator with integrated pulse-forming line for an ultra-wideband source," *J. Korean Phys. Soc.*, vol. 59, no. 61, pp. 3463–3467, Dec. 2011.

[13] B. Cadilhon, L. Pecastaing, T. Reess, and A. Gibert, "Low stray inductance structure to improve the rise-time of a Marx generator," *IET Electr. Power Appl.*, vol. 2, no. 4, pp. 248–255, 2008.

[14] B. Cadilhon *et al.*, "High pulsed power sources for broadband radiation," *IEEE Trans. Plasma Sci.*, vol. 38, no. 10, pp. 2593–2603, Oct. 2010, doi: 10.1109/TPS.2010.2042732.

[15] F. L. Song *et al.*, "Recent advances in compact repetitive high-power Marx generators," *Laser Part. Beams*, vol. 37, pp. 110–121, Mar. 2019, doi: 10.1017/S0263034619000272.

[16] T. Buntin *et al.*, "Compact Marx generator to drive a low-impedance MILO," in *Proc. IEEE Pulsed Power Plasma Sci. (PPPS)*, Jun. 2019, pp. 1–3, doi: 10.1109/PPPS34859.2019.9009681.

[17] C. J. Buchenauer, J. M. Pouncey, and J. M. Lehr, "Optimizing compact Marx generator networks for charging capacitive loads: Sequential triggering and practical considerations," in *Proc. IEEE Pulsed Power Plasma Sci. (PPPS)*, Jun. 2019, pp. 1–4, doi: 10.1109/PPPS34859.2019.9009950.

[18] *Computer Simulation Technology*. Accessed: Apr. 18, 2022. [Online]. Available: https://www.3ds.com/

[19] R. J. Adler, "Pulse power formulary," North Star Res. Corp., Albuquerque, NM, USA, Tech. Rep., 2001. [Online]. Available: http://www.dalitech.com/Resources/Pulse%20Power%20Formulary.pdf

[20] A. Zhabin, A. S. D. Ferron, L. Ariztia, M. Rivaletto, B. M. Novac, and L. Pecastaing, "Determination of breakdown voltage along the surface of a cylindrical insulator," *IEEE Trans. Dielectr. Electr. Insul.*, vol. 29, no. 1, pp. 327–333, Feb. 2022, doi: 10.1109/TDEI.2022.3148469.

[21] L. Li, Z. Huang, and Y. Yang, "The influence of electric field inhomogeneity on repetitive performance of a corona-stabilized switch," *IEEE Access*, vol. 8, pp. 195515–195527, 2020, doi: 10.1109/ACCESS.2020.3033327.

[22] E. I. Antipov, O. S. Belozerov, and E. G. Krastelev, "A high-current rail-type gas switch with preionization by an additional corona discharge," *Phys. At. Nuclei*, vol. 79, no. 14, pp. 1619–1624, 2016, doi: 10.1134/S1063778816140015.

[23] F. Mauseth, J. S. Jorstad, and A. Pedersen, "Streamer inception and propagation for air insulated rod-plane gaps with barriers," in *Proc. Annu. Rep. Conf. Electr. Insul. Dielectr. Phenomena*, Oct. 2012, pp. 732–739.

[24] J. C. Pouncey, J. M. Lehr, and D. V. Giri, "Erection of compact Marx generators," *IEEE Trans. Plasma Sci.*, vol. 47, no. 6, pp. 2902–2909, Jun. 2019, doi: 10.1109/TPS.2019.2915034.

[25] J. C. Pouncey and J. M. Lehr, "A parametric SPICE model for the simulation of spark gap switches," *Rev. Sci. Instrum.*, vol. 91, no. 3, Mar. 2020, Art. no. 034704.

[26] Y. Yao, I. V. Timoshkin, S. J. MacGregor, M. P. Wilson, M. J. Given, and T. Wang, "Postbreakdown transient characteristics of a gas-filled plasma closing switch," *IEEE Trans. Plasma Sci.*, vol. 49, no. 2, pp. 942–951, Feb. 2021, doi: 10.1109/TPS.2021.3053097.

[27] C. F. Wagner and A. R. Hileman, "Mechanism of breakdown of laboratory gaps," *Trans. Amer. Inst. Electr. Eng., III, Power App. Syst.*, vol. 80, no. 3, pp. 604–618, Apr. 1961, doi: 10.1109/AIEEPAS.1961.4501102.

[28] R. Pecquois *et al.*, "Simple and compact capacitive voltage probe for measuring voltage impulses up to 0.5 MV," *Rev. Sci. Instrum.*, vol. 83, no. 3, Mar. 2012, Art. no. 035001, doi: 10.1063/1.3690906.